Efficient solar-thermal energy conversion with surfactant-free Cu-oxide nanofluids

Hussein Sayed Moghaieb [a], Dilli Babu Padmanaban [a], Praveen Kumar [c], Atta Ul Haq [a], Chiranjeevi Maddi [a], Ruairi McGlynn [a], Miryam Arredondo [c], Harjit Singh [b], Paul Maguire [a], Davide Mariotti [a,*]

[a] Ulster University, School of Engineering, York Street, Belfast BT15 1AP, UK
[b] Institute of Energy Futures, College of Engineering, Design and Physical Sciences, Brunel University London, Uxbridge UB8 3PH, UK
[c] School of Mathematics and Physics, Queen's University Belfast, Belfast BT7 1NN, Northern Ireland, UK

ARTICLE INFO

ABSTRACT

High-specification nanofluids can potentially enable cost-effective and highly efficient solar-to-thermal energy conversion. However, their implementation is adversely affected by poor absorption spectral range and stability challenges of the nanoparticles. Here we demonstrate the synthesis, full characterization and application of Cu-oxide nanoparticles with high optical absorption and long-term stability over many months. The synthesis method, based on a hybrid plasma-liquid non-equilibrium electrochemical process, ensures a very limited environmental impact as it relies on a solid metal precursor while avoiding the use of additional chemicals such as surfactants and other reducing agents. We further investigate the fundamental links between the nanofluid performance and the material and optical properties and produce a theoretical model to determine the energy conversion efficiency. The results show that nanofluids produced with our Cu-oxide nanoparticles can achieve exceptional solar thermal conversion efficiencies close to ~90% and can provide a viable solution for an efficient solar thermal conversion technology.

1. Introduction

Modern society demands clean energy provision and complete reliance on renewable energy will require diversification of energy sources and technologies [1]. The conversion of solar energy into usable heat (e. g. domestic heating, hot water, industrial processes) represents an important component to this portfolio [2–5] and the potential exists to achieve reliable high conversion efficiencies, drastically reduce costs and radically simplify installation and maintenance thus bringing solar-thermal conversion technology to the fore en route to the decarbonization of energy production.

Dramatic progress in solar-thermal energy conversion requires the replacement of old engineering designs [6] with a new concept of direct absorbing solar collectors (DASCs) based on the use of nanofluids to enable light absorption volumetrically in the fluid without the use of inefficient intermediate absorbers [7] whereupon the generated heat is transported to where needed or to heat exchangers. Although this approach was originally considered by Minardi and Chuang in 1970's,

the absorbing fluids used dyes or micron-sized particles [8–10] and the technological implementation stalled significantly as rapid particle agglomeration, settling and/or dye degradation presented insurmountable obstacles [8,11–15] The adoption of specific nanofluids, with suitable materials design and synthesis, could dramatically improve the thermal properties of solar-thermal collectors and importantly yield absorption improvements in DASCs [14,16–24]. Advances in this field have been reported with important and promising results [25,26]. Aspects that relate to nanofluid preparation methods, optical and other properties as well as stability have been discussed [25,27]. The preparation and performance enhancement of nanofluids has included a range of techniques such as chemical, physical or plasma-based methodologies [25,27–29].

However, efforts to date to produce DASCs nanofluids have focused on nanostructures (e.g., carbon-based, metals, plasmonic and oxides) [9, 30,31], that have shown to suffer poor performance and were unable to meet the demanding requirements of light to heat conversions, colloidal and material stability, leaving substantial challenges to be overcome.

Research to date lacked a rigorous scientific investigation into the complex interrelationships and synergies involving nanomaterial optical and thermal properties, nanoscale solid-liquid interfaces, colloid stability and thermal or optically-induced materials degradation. Understanding nanofluid behaviour in this context is therefore of paramount importance to enable DASC technologies first, and then to enhance their performance and durability.

We have therefore studied a range of nanofluids that include plasmonic nanoparticles and carbon-based materials and here we report on the techniques and experimental approaches that we have developed leading to our best performing nanofluids, based on metal oxide nanoparticles. Metal oxide nanoparticles have so far been ignored for DASCs due to their poor absorption properties in the visible range; instead oxides have been only used for their wide-ranging chemical stability and to optimize nanofluid thermal properties in old solar-thermal collector designs [32–35]. Here we show that metal oxide nanoparticles can be the basis for the best performing DASC nanofluid, retaining thermal properties and chemical inertness whilst boosting solar-thermal conversion efficiency and stability.

We have synthesized surfactant-free Cu-oxide nanoparticles (CuOx NPs) with a hybrid plasma-induced non-equilibrium electrochemical (PiNE) process and provided full material characterization, identifying the morphology, crystal structure and chemical composition. Cu-oxide were chosen for several reasons, such as high thermal conductivity and high stability [34,36–38]. In addition, copper is abundantly available at low cost and have a limited environmental impact with low toxicity [35]. Our "green" synthesis method has been shown to produce stable dispersion of nanoparticles in liquid without the need for surfactant.[39–52] We have then studied our CuOx NPs optical properties in ethylene glycol-based nanofluids and linked their absorption and scattering behaviour to their fundamental material characteristics. We have further investigated the stability of our NPs over time (almost 1 year) and under repeated heat cycles.

2. Experimental section

2.1. Synthesis of the surfactant-free CuOx NPs

The setup used for the synthesis consists of a cell of two electrodes: a copper foil of 2 cm width, used as Cu precursor and as the sacrificial anode, and a nickel capillary tube (0.7 mm and 1 mm inner and outer diameter respectively) used to generate a microplasma, which serves as the cathode. The capillary tube is grounded through a ballast resistor of 100 kΩ and carries helium gas at approximately 1 mm above the solution surface. Photos and diagrams of the set-up are included in the Supplementary Information (S1). For the synthesis process, a 6-mL electrolyte was prepared using sodium chloride (NaCl), sodium nitrate (NaNO$_3$) and sodium hydroxide (NaOH) dissolved separately in distilled water (3 MΩ cm conductivity) at molar concentrations of 2.57 M, 15.3 mM, and 25 mM, respectively. The three solutions were mixed at a ratio of 1:1:1, i.e., 2 mL each, without using reducing, capping or stabilizing agents. The plasma was generated and sustained by applying an initial voltage of 2 kV and a constant direct current of 5 mA and discharging helium gas at a flow rate of 50 standard cubic cm (sccm). The plasma was generated at the surface of the electrolyte and sustained for 30 min treatment time; during this period, the voltage decreases to about 0.72 kV due to the increased conductivity of the solution while keeping the current constant. A gradual change in the solution colour from transparent to orange was observed during synthesis (S1, Supplementary Information). Immediately after synthesis, 6 × 6 mL as-prepared colloidal samples were loaded into two separate centrifuge tubes (three samples per tube for a total of 18 mL per tube) and centrifuged at 3000 revolution per minute (rpm) for three times in water followed by three more times in ethanol (50 mL each). The supernatant of each one of the two tubes was decanted, and a wet, dark brown precipitate was obtained and loaded into a glass vial for heat drying on a hotplate at

40 °C for 1 h. The total dry powder from both tubes was carefully weighed and shown to be 36 mg (i.e., ~6 mg per synthesized sample). Half of the collected powder, 18 mg, was transferred into a glass vial using a plastic spatula and annealed in an oven in air at 400 °C and for 6 h and then left to cool down by natural convection overnight. The annealed powder was completely black suggesting a phase transformation due to thermal oxidation (discussed in the main manuscript). Both powder samples, with annealed and not annealed CuOx NPs, were separately re-dispersed in EG at volume fractions of 0.001 vol%, 0.005 vol% and 0.01 vol%. The re-dispersion process was conducted through a bath-type sonicator (VWR USC300TH, 230 V, 50 Hz, 370 VA) for 2 h, followed by a probe-type sonicator (VCX-130PB ultrasonic processor, Sonics Materials) for 3 min at 80% (104 W) to achieve high dispersion homogeneity. The colloid samples in EG, from the annealed (AN) and not annealed (NA) powder, are the samples referred to as the nanofluid (NF) samples, which have been used throughout this work for characterization as well as performance analysis of solar-thermal conversion.

2.2. Materials characterization and optical properties

Scanning electron microscopy (SEM, HITACHI SU5000) was performed at an acceleration voltage of 10 kV, to check the surface morphology, size, and shapes of the CuOx NPs. Furthermore, the morphology and crystallinity of the CuOx NPs, before and after annealing, were investigated by transmission electron microscopy (TEM) including bright-field, centre dark-field imaging and selected area electron diffraction (SAED) performed on a Thermo Fisher Talos F200X G2 in TEM mode operated at 200 kV and equipped with a field emission gun cathode and four in-column super-X energy dispersive X-ray spectrometer (EDS) detectors having a total collection angle of ~0.9 sr. For TEM imaging, the samples were prepared by drop-casting a 20 μL droplet of each NF sample on a copper-coated carbon grid and left to dry overnight. For SEM, samples were prepared by drop-casting several droplets of each NF sample on a small piece of a silicon wafer, 0.5 cm × 0.5 cm, placed on a hot plate at 100 °C for drying. In addition, the crystal structure was examined by X-ray diffraction (XRD) with scans from 30° to 80°, with 0.01° increment, and 2 s/point. X-ray photoelectron spectroscopy (XPS) and reflection electron energy spectroscopy (REELS) were performed using the Thermo Scientific ESCALAB Xi+ spectrometer. Monochromatic Alkalpha X-ray source (hv= 1486.6 eV, 650 μm spot size) operated at a power of 225 W (15 kV and 15 mA) and the photoelectrons were collected using a 180° double focussing hemispherical analyser with dual detector system. The energy scale of the spectrometer was calibrated with sputter cleaned pure reference samples Au, Ag and Cu (Au4f7/2, Ag3d5/2 and Cu3p3/2) positioned at binding energies 83.96 eV, 368.21 eV and 932.62 eV, respectively. For all the samples analysed, the survey spectra were recorded with a step size of 0.1 eV and a pass energy of 20 eV. This pass energy gives a 0.65 eV width for the Ag 3d5/2 peak measured on a sputter cleaned Ag sample. REELS measurements were performed with a primary electron beam of energy of 1 keV. All the features were fully resolved with a pass energy of 10 eV and a step size of 0.1 eV, with an energy resolution of ~0.47 eV. Samples for XPS measurements were prepared in the same way as for SEM imaging. Moreover, transmittance and scattering spectra of the NF samples were measured using ultraviolet-visible-near infrared (UV-Vis-NIR) spectroscopy with an integrating sphere (LAMBDA 1050 +, PerkinElmer Inc.) over a wavelength range from 280 nm to 2500 nm using a standard quartz cuvette of 1 cm light path length. For the transmittance measurements an empty cuvette was used as reference as this approach allows for a direct comparison between the transmittance of EG and the nanofluids with limited errors. More details are provided in the Supplementary Information (S4) with regard to the measurements and calculations of the absorption and scattering coefficients.

3. Results and discussions

3.1. Nanoparticle synthesis, characterization and nanofluid preparation

The synthesis of surfactant-free copper oxide nanoparticles (CuOx NPs) was carried out with a custom-built system based on plasma-induced non-equilibrium electrochemistry (PiNE), see Supplementary Information-S1. PiNE has shown to be highly effective in initiating reactions at the liquid interface and leading to the synthesis of a wide range of nanomaterials, which would not be achievable using a standard electrode and without interfacing the plasma [47–52]. Specifically, the synthesis of metal oxides nanoparticles from a solid metal precursor has been reported and studied [49–55]. In this case, the solid precursor is expected to deliver Cu ions via anodic dissolution while plasma electron-induced dissociation contributes to the formation of water radicals; the interactions of these species can lead to a sol-gel process, which then evolves into forming nanoparticles [55]. The growth of the nanoparticles can be controlled by limiting the water content in the solution, as for instance ultra-small CuO quantum dots can be produced when PiNE is carried out in ethanol with only traces of water [55].

Full details of the synthesis steps and nanofluid preparation are given in the Methods section. Briefly, each PiNE synthesis process returns 6 mL of a water-based CuOx NP colloid, which is subsequently dried to yield 6 mg of dry CuOx NP powder. Some of the dry powder samples were subjected to a post-synthesis annealing step therefore producing two different types of samples, i.e., not annealed (NA) and annealed (AN) CuOx NPs. The CuOx NPs were then re-dispersed in ethylene glycol (EG) to form nanofluid (NF) samples with various concentrations corresponding to the NA and AN NPs, hereafter NA NF and AN NF, respectively.

To investigate the morphology and crystallinity of the CuOx NPs, we employed transmission electron microscopy (TEM) bright-field, centre dark-field imaging, and selective area electron diffraction (SAED) analysis as shown in Fig. 1a-d (NA CuOx NPs) and Fig. 1e-h (AN CuOx NPs). Bright-field and dark-field images yield diffraction contrast which is helpful in interpreting size, shapes, and defects in the CuOx NPs samples. Fig. 1a shows the bright-field image of the NA sample, a typical flower-like morphology could be identified resulting from several fingers (nanorod-like shape) of sizes up to 200 nm. Interestingly, small particles (mainly CuO) of sizes ranging from few nm to less than 15 nm are found in these nanorods, indicating that the nanorods consists of layers/sheets of CuO particles (Fig. 1c). High resolution images (Fig. 1d) confirm that particles are mainly CuO and are crystalline in nature, the fast Fourier transform (FFT) in the inset could be indexed with CuO (111) reflection. Fig. 1b represents the SAED pattern obtained on the NA CuOx NPs sample. We observed several diffraction rings emerging from the aggregates of the fingers (nanorods), these present random crystallographic orientations with a mixed phase composed of CuO (monoclinic) and Cu_2O (cubic) phases. The diffraction rings were indexed completely with the CuO (monoclinic) and Cu_2O (cubic) phases, while CuO being the dominating phase.

In contrast, annealed "AN" samples exhibit a different morphology, a typical nanosheet or multi-layer-structures can be seen in the image (Fig. 1e). The finger-like structure is somehow lost after the annealing as we observed fewer fingers and thicker areas due to layered-structures. SAED analysis (Fig. 1f) confirmed that the CuOx NPs are mainly composed of CuO (monoclinic) with small traces of Cu_2O phase. Another main difference is that AN samples contain large crystals (up to 100 nm), see the dark-field image using (220) reflections of CuO in Fig. 1g. Planar defects such as twinning were also observed in these large crystals (see bright-field image Fig. 1h) indicating the coalescence of CuOx NPs. This suggests that recrystallization of the small particles occurred during the annealing process. Additional TEM images are shown in the Supporting Information (Fig. S4), which include high-resolution TEM indicating the d spacings of 0.275 nm corresponding to (110) reflection of the CuO monoclinic structure. In summary, the annealing treatment induced a change in morphology of the CuOx NPs, due to coalescence of the CuOx NPs fingers (nanorod shape) resulting in a nanosheet or multi-layer-structures and where the small (< 15 nm) NPs have transformed into larger NPs. Moreover, the recrystallization of the small particles occurs in the AN sample yielding a predominantly pure CuO phase with minor traces of Cu_2O, however also creating widespread defects. These are important changes that we will show have impact on the optical properties of the NFs.

To further assess the macroscopic characteristics of the CuOx NPs, XRD scans were performed. As depicted in Fig. 2a, the XRD pattern of
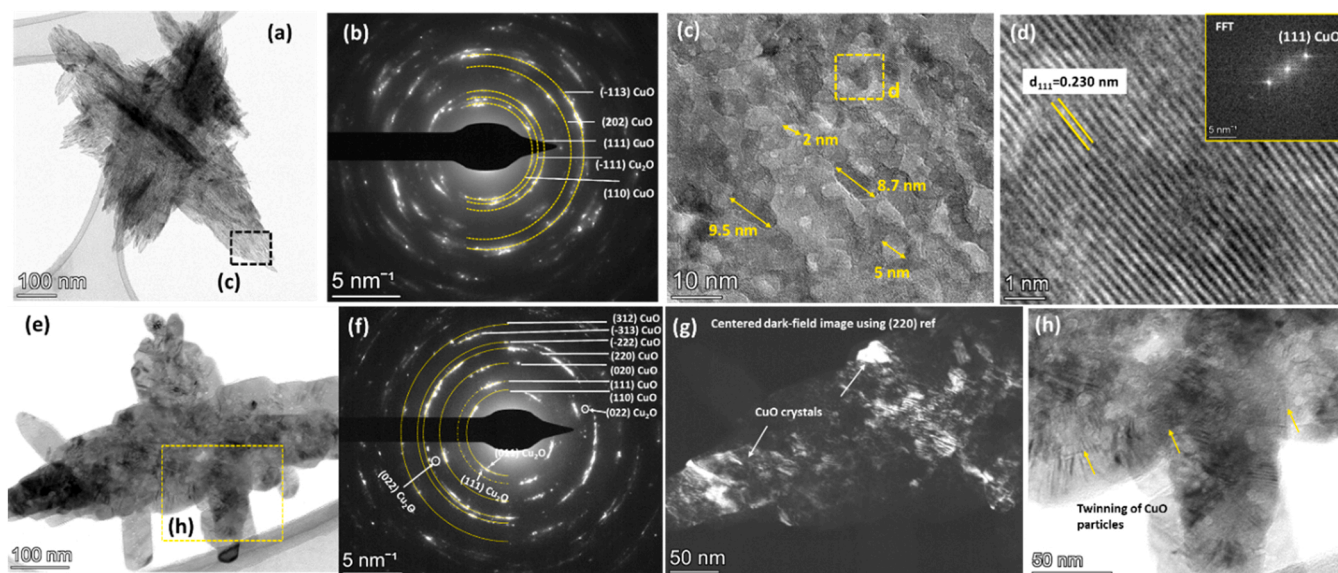
Fig. 1. TEM characterization of the not-annealed and annealed sf-CuOx NPs. **(a)** A low-magnification bright-field image. **(b)** The corresponding selected area electron diffraction (SAED) pattern of the CuO NPs in the not-annealed "NA" sample. **(c)** and **(d)** High-resolution images of the marked area in (a). Clearly, nanoparticles of sizes less than 15 nm are noticed in the images. **(e)** Overview bright-field image. **(f)** The corresponding SAED pattern of the CuO NPs recorded after annealing the sample "AN". **(g)** Centered dark-field image using (220) reflection of CuO showing crystals of up to 100 nm. **(h)** Enlarged view of the marked area in (e). Planar defects (follow the yellow arrows in (h) such as twinning can be noticed in the "AN" sample.
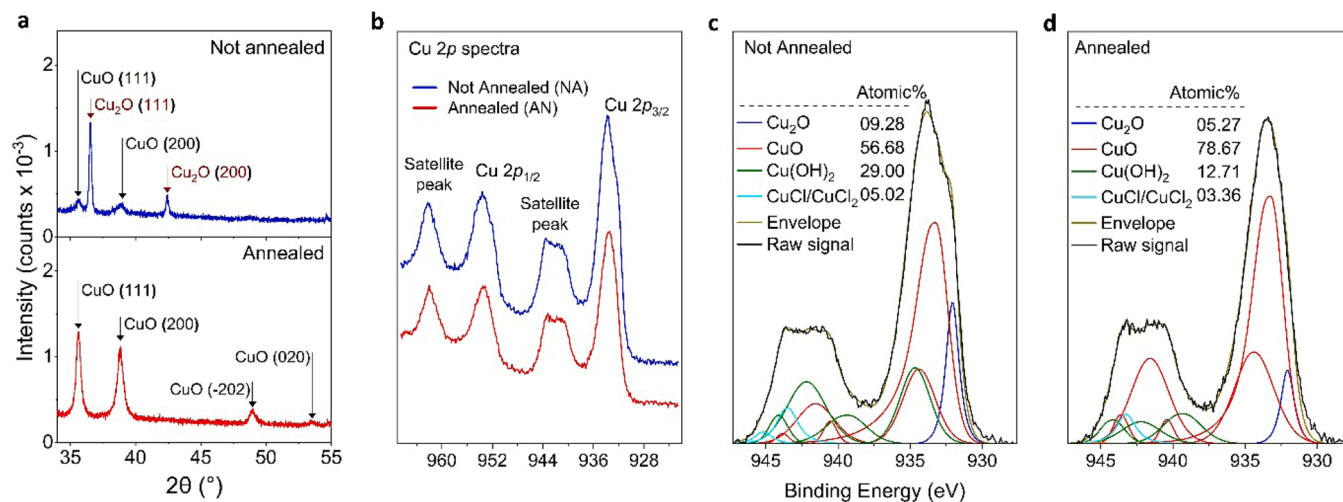
Fig. 2. XRD and XPS results of the not-annealed and annealed sf-CuOx NPs. **(a)** XRD spectra showing the peaks identification of CuOx NPs for the not annealed and the annealed sample. **(b)** XPS results of CuOx NPs showing the Cu 2p and shoulder peaks. **(c)** Deconvolution of the Cu $2p_{3/2}$ region of the not-annealed "NA" sample using the Thermo Scientific™ Avantage Software. **(d)** Deconvolution of the Cu $2p_{3/2}$ region of the annealed "AN" sample using the Thermo Scientific™ Avantage Software.

the NA CuOx NPs contains two mixed phases of Cu_2O and CuO. The highest peak is located at a 2θ angle of $36.11°$ assigned to the (111) plane of Cu_2O. Another peak corresponding to Cu_2O can also be found at $\sim43°$ and assigned to the (200) plane. Two small peaks originating from CuO (200) and (−202) are also observed. The AN sample features only peaks corresponding to the CuO phase. Fitting of the spectra (S3 Supplementary Information) reveals that the AN sample is pure CuO, while before annealing the Cu_2O phase was predominant.

Chemical composition of the CuOx NPs was analysed by X-ray photoelectron spectroscopy (XPS) of both NA and AN samples (Fig. 2b-d) to provide a more sensitive and detailed analysis of the surface. As shown in Fig. 2b, the Cu 2p spectra of both samples are composed of two main characteristic peaks, i.e., Cu $2p_{3/2}$ and Cu $2p_{1/2}$ with binding energies of 933.8 eV and 953.8 eV, respectively [56–58]. In addition, the existence of a strong shake-up satellites of Cu(II), resulting from multiple excitations on the oxide surface, confirms that CuO is predominant in the samples [59]. Cu $2p_{3/2}$ and the corresponding shoulder peak were fitted according to relevant literature (table 4 in ref. [60]). Peaks representing the bonds in CuO, Cu_2O, $Cu(OH)_2$ and $CuCl/CuCl_2$ were included (Fig. 2b-d). The percentage of the CuO phase went from 57% in the NA sample to 79% in the AN sample. In addition, the decrease in the

percentage of the Cl-based impurities from 5% to 3% resulting from their degradation at high temperature, also contributed to the increase in CuO [61,62]. showing the benefit of heat treatment in purifying the NA CuOx NPs. The decrease of the $Cu(OH)_2$ component from 29% to 13% is consistent with OH terminations at the NPs surface and also in agreement with the decrease of the overall surface area with increasing particle dimension. The differences between the composition percentages determined by XRD with those obtained from XPS are due to the XRD probing the bulk of the samples, while XPS provides a surface characterization. However, both sets of results confirm the phase transformation from Cu_2O to CuO resulting in the annealed sample being formed for the most part of the CuO phase.

3.2. Optical properties of the nanofluids

The transmittance spectra of EG and the CuOx/EG NFs at different volume fractions were measured over the wavelength range 300–2500 nm which makes up 99.3% of the solar irradiance (992.6 W/ m^2) [63]. As can be seen from Fig. 3a, EG is a strong absorber in the near infrared (NIR) region at wavelengths above 1350 nm but is mostly transparent below that. In particular, EG transmittance is above 90% in
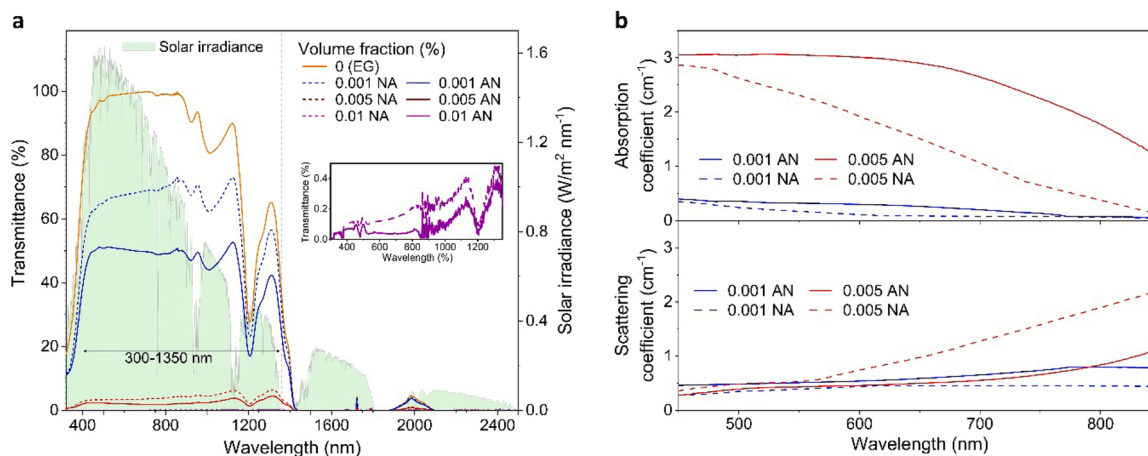
Fig. 3. Optical properties of the not-annealed and annealed sf-CuOx NPs. **(a)** UV-Vis-IR transmittance spectra of CuOx/EG nanofluids. The inset gives a clear view of the very low transmittance signal of the highest concentration, 0.01 vol%, (NA and AN) which is close to the instrument noise. **(b)** Coefficients of absorption and scattering of the CuOx/EG nanofluids, annealed (AN) and not annealed (NA).

the range 450–950 nm, where the NFs are therefore expected to efficiently absorb most of the radiation. For our NFs, the introduction of the CuOx NPs into EG drastically reduces the transmittance across the full range not covered by EG (Fig. 3a, 300–1350 nm). This reaches NF transmittance below 10% across the full wavelength range even with a concentration as low as 0.005 vol%, while the 0.01 vol% exhibited near-zero transmittance at the limit of the system noise (inset Fig. 3a).

As the transmittance measurements represent only a partial picture of the solar-thermal conversion process, we have then taken measurements with an integrating sphere and we have calculated the absorption and scattering coefficients for the NFs at the different CuOx NP concentrations (Section S4, Supplementary Information). Here we have not considered the highest concentration (0.01 vol%) because the transmittance measurement values were too low to allow the calculation of the absorption and scattering coefficients. Fig. 3b clearly shows that all nanofluids exhibited high and broad absorption coefficients over the wavelength range of interest, (450–950 nm) with the highest values in the visible region. It can be also seen that the absorption significantly increased with increasing the concentration up to 0.005 vol%. In addition, the heat treatment greatly enhances the absorption coefficient (Annealed-AN samples, solid lines in Fig. 3b). For instance, within the range 450–950 nm that covers ~61% of the solar irradiance, the absorption coefficient at a volume fraction of 0.005% of the NA nanofluid dropped almost linearly from 2.9 cm^{-1} to a much lower value of 0.27 cm^{-1}, but when the annealed-AN NPs were used at the same concentration and within the same wavelength range, the absorption coefficient was above 3 cm^{-1} from 450 nm to 630 nm and then dropped reaching values still above 1 cm^{-1} at 950 nm. NFs exhibited increased scattering with increasing the wavelength and became stronger for the two higher concentrations at wavelengths above 750 nm, where they poorly absorb, while the lower concentration showed constant scattering over the entire range. However, the NFs with the AN CuOx NPs, particularly at 0.05 vol%, exhibited a much lower scattering than that of the samples containing the powder that was not annealed (NA NFs) confirming the benefits of the annealing in terms of reducing losses that could originate from scattering.

The increased absorptivity for the AN NFs with respect to the samples that were not annealed can be in part attributed to the "purification" of the Cu-oxide phase from Cu_2O to CuO, where CuO is known to have a lower bandgap (1.2 eV) [64] and therefore a larger absorption range (S5, Supplementary Information). The samples that were annealed show a fairly high phase purity as confirmed by TEM, XRD and XPS. Furthermore, as per our TEM analysis, the NA CuOx NPs include very small CuO NPs (<15 nm, Fig. 1c) which are not present in the AN samples. CuO of such small diameter is to be considered under strong quantum confinement and is expected to exhibit a bandgap well above 2 eV [49]. However, the absorption coefficient of the AN NFs presents a clear different trend above 500 nm compared to the NF with NPs that were not annealed (Fig. 3b) and defect states may have also contributed to this. Indeed, our TEM analysis have indicated an increase of the defect density in the AN CuOx NPs (Fig. 1h).

3.3. Nanofluid solar-thermal conversion efficiency & computational 3D model

We have studied how the optical properties lead to solar-thermal conversion and have evaluated the corresponding conversion efficiency. A description of the experimental set-up used is provided in the Supplementary Information (S6). We used a solar simulator with light intensity of approximately 1000 W/m^2 and 940 W/m^2 reaching the NF surface since the fused quartz cover has transmittance of 94% (S9, Supplementary Information). The temperature variation of the NF samples was recorded until thermal equilibrium. As depicted in Fig. 4a, all nanofluids exhibited a faster temperature increase through the first few minutes, during which the heat loss rate was not significant since the temperature difference between the nanofluid and the ambient air and surrounding walls is relatively small. With the rise in nanofluid temperature, heat loss became significant and continued to increase until thermal equilibrium was reached. It can be also seen that increasing the concentration resulted in a significant enhancement in temperature rise. For each concentration, the temperature rise achieved with AN NFs was greater than those of NA NFs, Fig. 4a.

While these experimental results provide important qualitative information, in order to determine the STC efficiency, a model needs to be developed to take into account all the heat transfer losses and light interactions at interfaces etc. Hence, the results shown in Fig. 4a are then used to validate a 3-D steady-state model that was implemented in ANSYS® Fluent using the discrete ordinates (DO) method for non-grey
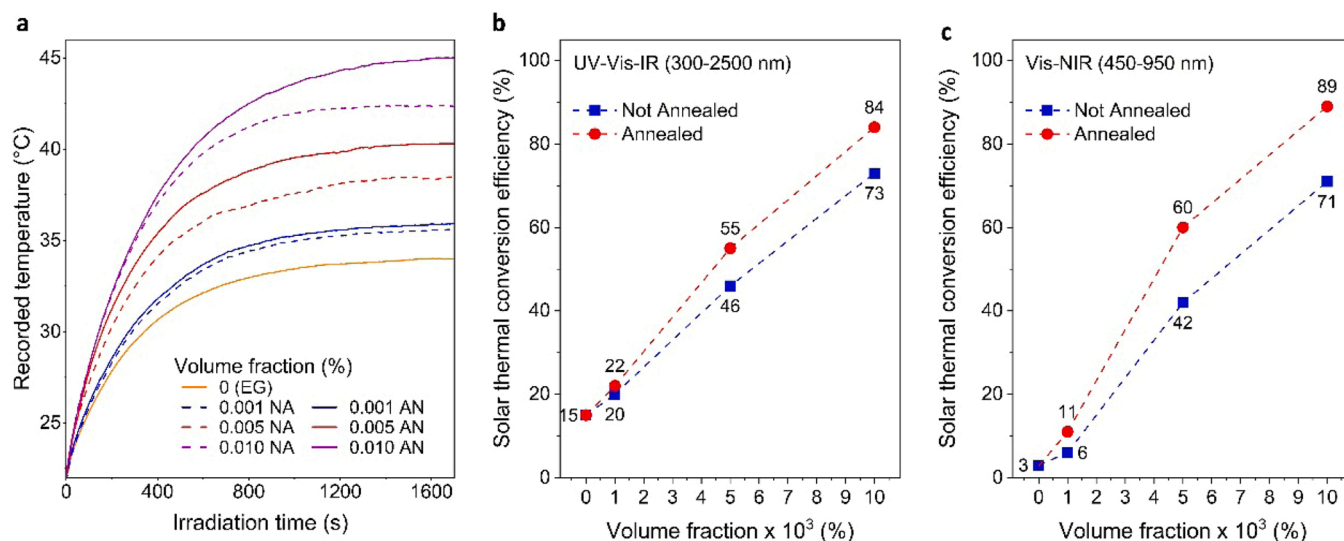
Fig. 4. Experimental results of the solar-thermal energy conversion of sf-CuOx/EG nanofluids and validation of the numerical model. (a) Experimental transient temperature followed by the steady-state temperature at thermal equilibrium of EG and NA and AN CuOx/EG NFs under solar irradiation of one sun (3.5-mm sample depth without using thermal insulation). (b) Steady-state solar thermal conversion efficiency of the not-annealed "NA" and annealed "AN" CuOx/EG NFs at different volume fractions over the UV-Vis-IR region (300–2500 nm), which make up 99.3% of the solar power (992.6 W/m^2) at AM1.5 [63]. (c) Steady-state solar thermal conversion efficiency of the not-annealed "NA" and annealed "AN" CuOx/EG NFs at different volume fractions over the Vis-NIR region (450–950 nm) which make up 60.7% of the solar power (992.6 W/m^2) at AM1.5 [63].

participating media (Section S7, Supplementary Information). The model allows us to gain insights into the spatial distribution of the energy transfer processes, temperature gradients and to have an accurate estimation of the NF solar-thermal conversion (STC) efficiency. In order to determine the STC efficiency we have evaluated the transient behaviour and solved for an arbitrary period of irradiation time (ten minutes) with thermally insulated NF and by applying adiabatic boundary conditions to all NF surfaces. Under these conditions the rates of temperature change over time and the STC efficiency did not change considerably across the NF volume (see Supplementary Information, Fig. S16b).

As illustrated in Fig. 4b, simulating a 3.5 mm deep NF, EG exhibited 15% STC efficiency, owing primarily to its UV and IR absorption, with only 2.8% absorption in the Vis-NIR region (Fig. 4c). With the addition of CuOx/EG NPs, the efficiency increased to 20% and 22% for the NA and AN samples, respectively, at 0.001 vol% (Fig. 4b). They, however, performed poorly in the Vis-NIR region with only 6% and 11% respectively (Fig. 4c), owing to their low absorption in this region (see Fig. 3b). At higher concentrations within the UV-Vis-IR spectra, the efficiency was enhanced significantly, reaching 46% and 55% for the NA and AN samples of 0.005 vol%, respectively, which further increased at 0.01 vol % to reach values of 73% and 84% for the NA and AN samples, respectively (Fig. 4b). In the Vis-NIR region at higher concentrations, NA sample efficiency decreased compared to UV-Vis-IR, while the AN sample efficiency reached their maximum of 89% for 0.01 vol% (Fig. 4c). This may be attributed to reduced scattering with AN samples at high concentration compared to NA, Fig. 3b.

Simulations of AN NFs with different depths were carried out and the total absorbed power, temperature and thermal conversion efficiency versus depth are quantified, Fig. 5. At the higher concentrations, ~90% of the total power is absorbed by nanofluids with only 10 mm depth, Fig. 5a, while EG has absorbed < 30% of the total solar power at the same depth. At lower concentrations > 50% of the solar power is absorbed by nanofluid with a 10 mm depth. Simulations also show that high concentration samples with a depth of 10 mm or less, after 600 s, surface temperatures can reach 60–100 °C, falling to near ambient when a depth of 7 mm is used, Fig. 5b. The solar thermal conversion efficiency peaks for nanofluid with a depth of ~3.5–5 mm, with a maximum of 89% (0.01 vol%), Fig. 5c. When the samples with a shallow depth are used, the efficiency is lower, as illustrated in Fig. 5; this is because some of the solar power is not absorbed and it is transmitted through the full depth of the samples. On the other hand, increasing the depth beyond

the values that produce the highest efficiency, i.e. above 4–5 mm, the volumetric power density is reduced; in other words, when the depth exceeds the optimal values, a fraction of the nanofluid volume at the bottom of the sample is not contributing to the absorption as most of the solar power has been already absorbed in the top part of the sample. Our model could therefore be used to optimize operating conditions for different deployment scenarios through adjusting the fluid depth, geometry and concentration.

3.4. Stability of the nanofluids

Nanofluids stability and its characterisation is of major importance. We have monitored the colloidal stability of AN and NA static samples (0.005%), via transmittance measurement, for 30 days at room temperature and with up to 20 one-hour heating cycles at 90 °C.

Fig. 6a shows that the transmittance variation with time which indicates a very slow sedimentation of the CuOx NPs, with the annealed samples displaying a lower sedimentation rate. Under realistic operating conditions, nanofluids are continuously re-circulated. Manual shaking of stored samples (30 days) for a few seconds was sufficient to restore the original Day 0 transmittance. Note that the D0 data and 'After shaking' data completely overlap in Fig. 6a. AN and NA samples (0.005 vol%) were subjected to 90 °C thermal cycling to test the impact on stability (Fig. S17, Supplementary Information). After 20 heating cycles, little change in the transmittance spectra (Fig. 6b) and absorption coefficient (Fig. 6c) has occurred with a maximum decrease in the absorption coefficient of 8% (at 480 nm) and 4% (at 590 nm) for NA and AN samples respectively, indicating a high degree of thermal stability.

Our nanofluids show exceptional stability under heat cycles that can be ascribed to the inorganic oxide phase of our NPs and the absence of any ligand or surfactant. This is because inorganic oxides are expected to be highly stable for a wide range of temperatures, while the use of organic materials, ligands or surfactant can easily degrade at relatively low temperatures. Furthermore, surfactants, in addition to compromising the optical properties, can introduce a high thermal resistance at the NP-liquid interface hence further increasing the temperature at the surfactant organic components. The absence of specific surfactants can however negatively impact the long-term stability and while the long-term static stability of our NFs have outperformed some of the nanofluids reported in the literature [65–67] they have also shown poorer long-term static stability when compared to some other nanofluids that have used organic or functionalized NPs [27,68–72]. We should
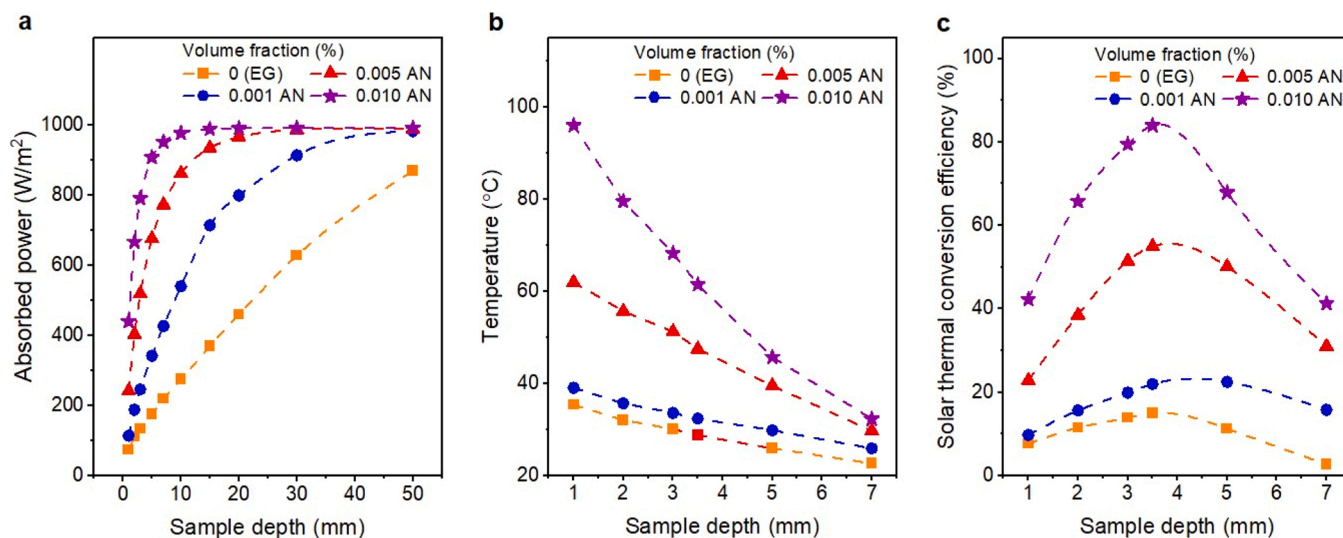

Fig. 5. Numerical model results of the solar-thermal energy conversion of sf-CuOx/EG nanofluid. (a) The effect of varying the depth of annealed "AN" CuOx/EG NFs on the absorbed power. (b) The effect of varying the depth of annealed "AN" CuOx/EG NFs on the temperature obtained at the midpoint of each sample depth. (c) The corresponding solar-thermal energy conversion efficiency. A parametric study was carried out to determine these three varying parameters at each depth.
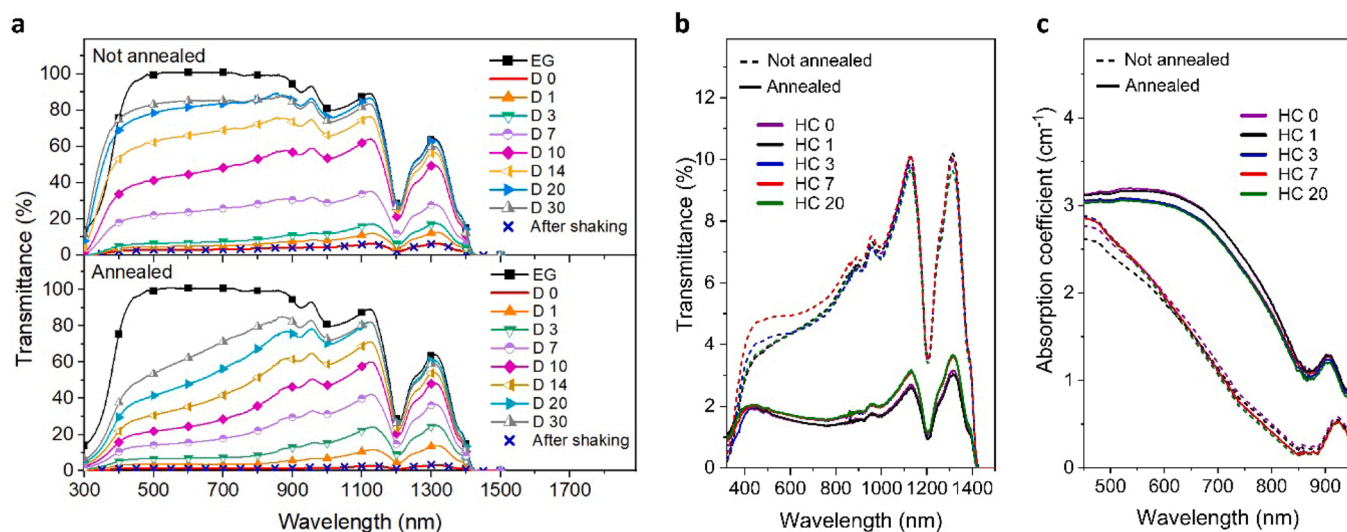
Fig. 6. Physical and thermal stability of sf-CuOx/EG nanofluids. **(a)** Transmittance measurements at different days (D) for the not-annealed "NA" and annealed "AN" CuOx NFs at 0.005 vol%. Samples were not shaken, and measurements were taken to observe settling in static mode (D 0 to D 30). After more than 300 days, the sample was shaken by hand ("after shaking") and transmittance measurements were carried out. Note that the data at D0 and "after shaking" overlap completely. **(b)** Effect of heat cycles (HCs) on the transmittance of CuOx/EG nanofluids at 0.005 vol% for both the NA and AN. **(c)** Effect of HCs on the absorption coefficient of CuOx/EG nanofluids at 0.005 vol% for both the NA and AN.

however note that many performance measurements in the literature do not report sufficient details for a comprehensive comparison and in some cases working fluids that are ultimately not suitable for DASCs have been used [27,65,66,68,69,72]. As expected, due to the surfactant opto-thermal properties and degradation, when the thermal stability and the energy conversion efficiency of such functionalized/organic-based nanofluids have been assessed, these have presented poorer outcomes than our NFs [27,28,68,70,71]. Hence, the assessment of DASCs nanofluids needs to take into consideration the operational conditions and consider the wider range of performance parameters such as energy conversion efficiency, thermal stability as well as static and '*dynamic*' stability and where a trade-off may be required. Further work will be required in the development of optimal DASC nanofluids where the compromise between solar-to-thermal energy conversion efficiency and stability parameters can be minimized.

Overall, these results show that our NFs exhibit suitable stability and continued exceptional energy conversion performance under a range of important realistic operational conditions. These characteristics can be attributed to the optical and thermal properties as well as chemical stability of metal oxide and CuO more specifically. The OH-terminations that we observed in the CuOx NPs may have also contributed to the exceptional stability.

4. Conclusion

We have shown that a judicious and rigorous investigation from material synthesis to application and modelling can deliver high performance materials for solar-thermal energy conversion. Our results show that combining PiNE synthesis with a subsequent annealing step can produce NPs with suitable morphology, crystal structure, purity and surface characteristics. We have in this case shown that narrow size distributions and control over specific morphologies are not required to improve the nanofluid macroscopic properties. Our nanofluids with CuOx NPs have exhibited a broad and strong absorption range that covers the UV-Vis-NIR spectrum which complements the EG absorption spectra at longer wavelengths. Furthermore, we have been able to verify their stability against sedimentation for many months and for 90 ºC thermal cycling. The solar to thermal energy conversion efficiency increases with NP concentration, from < 20% for EG only up to ~90% for CuOx - EG nanofluids at a nanoparticle concentration of 0.01 vol%. This

exceptional increase in efficiency demonstrates that almost all solar energy can be potentially converted into heat with appropriate optimization of materials, concentration and collector geometry.

CRediT authorship contribution statement

Hussein Sayed Moghaieb: Conceptualization, Methodology, Validation, Formal analysis, Software, Investigation, Writing – original draft, Writing – review & editing, Visualization. **Dilli Babu Padmanaban:** Validation, Formal analysis, Investigation, Writing – review & editing, Visualization. **Praveen Kumar:** Methodology, Validation, Formal analysis, Investigation, Writing – original draft, Writing – review & editing, Visualization. **Atta Ul Haq:** Validation, Formal analysis, Investigation, Writing – review & editing, Visualization. **Chiranjeevi Maddi:** Validation, Formal analysis, Investigation, Writing – review & editing. **Ruairi McGlynn:** Validation, Formal analysis, Investigation, Writing – review & editing. **Miryam Arredondo:** Methodology, Formal analysis, Resources, Data curation, Writing – original draft, Writing – review & editing, Visualization, Project administration, Funding acquisition. **Harjit Singh:** Writing – review & editing, Validation, Formal analysis. **Paul Maguire:** Resources, Writing – review & editing, Project administration, Funding acquisition. **Davide Mariotti:** Conceptualization, Methodology, Formal analysis, Resources, Data curation, Writing – original draft, Writing – review & editing, Visualization, Project administration, Funding acquisition.

Declaration of Competing Interest

The authors declare that they have no known competing financial interests or personal relationships that could have appeared to influence the work reported in this paper.

Data Availability

Data will be made available on request.

Acknowledgments

McFarland for carrying out XRD measurements.

Appendix A. Supporting information

Supplementary data associated with this article can be found in the online version at doi:10.1016/j.nanoen.2022.108112.

References

[1] D. Welsby, J. Price, S. Pye, P. Ekins, Unextractable fossil fuels in a 1.5 °C world, Nature 597 (7875) (2021) 230–234, https://doi.org/10.1038/s41586-021-03821-8.
[2] J.A. Duffie, W.A. Beckman, Solar Engineering of Thermal Processes, fourth ed., John Wiley & Sons, 2013.
[3] I.M. Mahbubul, M.M.A. Khan, N.I. Ibrahim, H.M. Ali, F.A. Al-Sulaiman, et al., Carbon nanotube nanofluid in enhancing the efficiency of evacuated tube solar collector, Renew. Energy 121 (2018) 36–44.
[4] T. Yousefi, F. Veysi, E. Shojaeizadeh, S. Zinadini, An experimental investigation on the effect of Al2O3–H2O nanofluid on the efficiency of flat-plate solar collectors, Renew. Energy [Internet] 39 (1) (2012) 293–298, https://doi.org/10.1016/j.renene.2011.08.056 (Available from), ⟨http://www.sciencedirect.com/science/article/pii/S0960148111005180⟩.
[5] A.G. Lupu, V.M. Homutescu, D.T. Balanescu, Popescu A. Efficiency of solar collectors–a review. IOP Conference Series: Materials Science and Engineering, IOP Publishing, 2018, p. 82015.
[6] P. Tao, G. Ni, C. Song, W. Shang, J. Wu, J. Zhu, et al., Solar-driven interfacial evaporation, Nat. Energy 3 (12) (2018) 1031–1041.
[7] J.E. Minardi, H.N. Chuang, Performance of a "black" liquid flat-plate solar collector, Sol. Energy 17 (3) (1975) 179–183.
[8] E. Sani, L. Mercatelli, S. Barison, C. Pagura, F. Agresti, L. Colla, et al., Potential of carbon nanohorn-based suspensions for solar thermal collectors, Sol. Energy Mater. Sol. Cells 95 (11) (2011) 2994–3000, https://doi.org/10.1016/j.solmat.2011.06.011.
[9] T.R. Shah, H.M. Ali, Applications of hybrid nanofluids in solar energy, practical limitations and challenges: a critical review, Sol. Energy 183 (2019 1) 173–203, https://doi.org/10.1016/J.SOLENER.2019.03.012.
[10] B.-J.J. Huang, T.-Y.Y. Wung, S. Nieh, Thermal analysis of black liquid cylindrical parabolic collector, Sol. Energy 22 (3) (1979 1) 221–224, https://doi.org/10.1016/0038-092X(79)90136-1.
[11] W. Chamsa-Ard, S. Brundavanam, C.C. Fung, D. Fawcett, G. Poinern, Nanofluid types, their synthesis, properties and incorporation in direct solar thermal collectors: a review, Nanomaterials (Basel) 7 (6) (2017) 131.
[12] J. Kirk Cochran HJB and PLY. Encyclopedia of Ocean Sciences. third. 2019. 4306 p.
[13] A.K. Sinha, P.K. Manna, M. Pradhan, C. Mondal, S.M. Yusuf, T. Pal, Tin oxide with ap–n heterojunction ensures both UV and visible light photocatalytic activity, RSC Adv. 4 (1) (2014) 208–211.
[14] T.P. Otanicar, P.E. Phelan, J.S. Golden, Optical properties of liquids for direct absorption solar thermal energy systems, Solar Energy 83 (7) (2009) 969–977.
[15] R. Jiang, S. Cheng, L. Shao, Q. Ruan, J. Wang, Mass-based photothermal comparison among gold nanocrystals, PbS nanocrystals, organic dyes, and carbon black, J. Phys. Chem. C. 117 (17) (2013) 8909–8915.
[16] Choi S.U.S., Eastman J.A. Enhancing thermal conductivity of fluids with nanoparticles. Argonne National Lab., IL (United States); 1995.
[17] B.J. Lee, K. Park, T. Walsh, L. Xu, Radiative heat transfer analysis in plasmonic nanofluids for direct solar thermal absorption, J. Solar Energy Eng. 134 (2) (2012).
[18] T.P. Otanicar, P.E. Phelan, R.S. Prasher, G. Rosengarten, R.A. Taylor, energy sustainable. Nanofluid-based direct absorption solar collector, J. Renew. Energy Sustain. 2 (3) (2010) 33102.
[19] Z. Luo, C. Wang, W. Wei, G. Xiao, Performance improvement of a nanofluid solar collector based on direct absorption collection (DAC) concepts, Int. J. Heat Mass Transf. 75 (2014) 262–271.
[20] K. Garg, V. Khullar, S.K. Das, H. Tyagi, Parametric study of the energy efficiency of the HDH desalination unit integrated with nanofluid-based solar collector, J. Therm. Anal. Calorimetr. 135 (2) (2019) 1465–1478.
[21] S. Dugaria, M. Bortolato, D.D. Col, Modelling of a direct absorption solar receiver using carbon based nanofluids under concentrated solar radiation, Renew. Energy 128 (2018) 495–508.
[22] Zhu Q., Li Y., Mu L., Cui Y. Theoretical investigation of radiative transport and heat transfer of nanofluids in a direct solar absorption collector. In: International Heat Transfer Conference. 2010. p. 877–82.
[23] S. Delfani, M. Karami, M.A. Akhavan-Behabadi, Performance characteristics of a residential-type direct absorption solar collector using MWCNT nanofluid, Renew. Energy 87 (2016) 754–764.
[24] O. Mahian, E. Bellos, C.N. Markides, R.A. Taylor, A. Alagumalai, L. Yang, et al., Recent advances in using nanofluids in renewable energy systems and the environmental implications of their uptake, Nano Energy 86 (2021), 106069, https://doi.org/10.1016/J.NANOEN.2021.106069.
[25] R. Taylor, S. Coulombe, T. Otanicar, P. Phelan, A. Gunawan, W. Lv, et al., Small particles, big impacts: a review of the diverse applications of nanofluids, J. Appl. Phys. 113 (1) (2013) 1.
[26] A. Ghadimi, R. Saidur, H.S.C. Metselaar, A review of nanofluid stability properties and characterization in stationary conditions, Int. J. Heat. Mass Transf. [Internet] 54 (17) (2011) 4051–4068, https://doi.org/10.1016/j.
ijheatmasstransfer.2011.04.014 (Available from), ⟨https://www.sciencedirect.com/science/article/pii/S0017931011002304⟩.
[27] N. Hordy, D. Rabilloud, J.-L. Meunier, S. Coulombe, High temperature and long-term stability of carbon nanotube nanofluids for direct absorption solar thermal collectors, Sol. Energy 105 (2014) 82–90.
[28] J. Tavares, S. Coulombe, Dual plasma synthesis and characterization of a stable copper–ethylene glycol nanofluid, Powder Technol. 210 (2) (2011) 132–142.
[29] D. Vollath, Plasma synthesis of nanoparticles, Kona Powder Part. J. 25 (2007) 39–55.
[30] N. Chen, H. Ma, Y. Li, J. Cheng, C. Zhang, D. Wu, et al., Complementary optical absorption and enhanced solar thermal conversion of CuO-ATO nanofluids, Sol. Energy Mater. Sol. Cells 162 (2017) 83–92, https://doi.org/10.1016/J.SOLMAT.2016.12.049.
[31] J. Sarkar, P. Ghosh, A. Adil, A review on hybrid nanofluids: recent research, development and applications, Renew. Sustain. Energy Rev. 43 (2015) 164–177, https://doi.org/10.1016/j.rser.2014.11.023.
[32] Q. Xiong, A. Hajjar, B. Alshuraiaan, M. Izadi, S. Altnji, S.A. Shehzad, State-of-the-art review of nanofluids in solar collectors: a review based on the type of the dispersed nanoparticles, J. Clean. Prod. 310 (2021), 127528, https://doi.org/10.1016/J.JCLEPRO.2021.127528.
[33] M. Liu, M. Lin, I. Huang, C. Wang, Enhancement of thermal conductivity with CuO for nanofluids, Chem. Eng. Technol.: Ind. Chem. Equip. Eng. -Biotechnology 29 (1) (2006) 72–77.
[34] A. Qiang, L. Zhao, C. Xu, M. Zhou, Effect of dispersant on the colloidal stability of nano-sized CuO suspension, J. Dispers. Sci. Technol. 28 (7) (2007) 1004–1007.
[35] L. Zhang, Q. Feng, A. Nie, J. Liu, H. Wang, Y. Fang, In situ study of thermal stability of copper oxide nanowires at anaerobic environment, J. Nanomater (2014) 2014.
[36] S. Ghosh, T. Liu, M. Bilici, J. Cole, I.-M. Huang, D. Staack, et al., Atmospheric-pressure dielectric barrier discharge with capillary injection for gas-phase nanoparticle synthesis, J. Phys. D Appl. Phys. 48 (31) (2015), 314003.
[37] Y. Yang, D. Xu, Q. Wu, P. Diao, Cu 2 O/CuO bilayered composite as a high-efficiency photocathode for photoelectrochemical hydrogen evolution reaction, Sci. Rep. 6 (2016) 35158.
[38] X. Zhang, J. Qiu, X. Li, J. Zhao, L. Liu, Complex refractive indices measurements of polymers in visible and near-infrared bands, J. Quant. Spectr. Radiat. Transf. 59 (8) (2020) 2337–2344.
[39] J. McKenna, J. Patel, S. Mitra, N. Soin, V. Švrček, P. Maguire, et al., Synthesis and surface engineering of nanomaterials by atmospheric-pressure microplasmas, Eur. Phys. J. -Appl. Phys. 56 (2) (2011).
[40] D. Mariotti, R.M. Sankaran, Perspectives on atmospheric-pressure plasmas for nanofabrication, J. Phys. D. Appl. Phys. 44 (17) (2011), 174023.
[41] D. Mariotti, R.M. Sankaran, Microplasmas for nanomaterials synthesis, J. Phys. D: Appl. Phys. 43 (32) (2010), 323001.
[42] Saito G., Akiyama T. Nanomaterial Synthesis Using Plasma Generation in Liquid. Chen W, editor. J Nanomater. 2015;2015:123696. DOI:10.1155/2015/123696.
[43] A. Khlyustova, N. Sirotkin, A. Kraev, V. Titov, A. Agafonov, Plasma–liquid synthesis of MoO x and WO 3 as potential photocatalysts, Dalton Trans. 49 (19) (2020) 6270–6279.
[44] G. Xu, W. Chen, S. Deng, X. Zhang, S. Zhao, Performance evaluation of a nanofluid-based direct absorption solar collector with parabolic trough concentrator, Nanomaterials (Basel) 5 (4) (2015) 2131–2147.
[45] W. Chiang, D. Mariotti, R.M. Sankaran, J.G. Eden, K. Ostrikov, Microplasmas for advanced materials and devices, Adv. Mater. 32 (18) (2020), 1905508.
[46] Y. Shimizu, A.C. Bose, D. Mariotti, T. Sasaki, K. Kirihara, T. Suzuki, et al., Reactive evaporation of metal wire and microdeposition of metal oxide using atmospheric pressure reactive microplasma jet, Jpn J. Appl. Phys. 45 (10S) (2006) 8228.
[47] J. Patel, L. Němcová, P. Maguire, W.G. Graham, D. Mariotti, Synthesis of surfactant-free electrostatically stabilized gold nanoparticles by plasma-induced liquid chemistry, Nanotechnology 24 (24) (2013), 245604.
[48] R.-C. Zhang, D. Sun, R. Zhang, W.-F. Lin, M. Macias-Montero, J. Patel, et al., Gold nanoparticle-polymer nanocomposites synthesized by room temperature atmospheric pressure plasma and their potential for fuel cell electrocatalytic application, Sci. Rep. 7 (1) (2017) 1–9.
[49] T. Velusamy, A. Liguori, M. Macias-Montero, D.B. Padmanaban, D. Carolan, M. Gherardi, et al., Ultra-small CuO nanoparticles with tailored energy-band diagram synthesized by a hybrid plasma-liquid process, Plasma Process. Polym. 14 (7) (2017), 1600224.
[50] A. Liguori, T. Gallingani, D.B. Padmanaban, R. Laurita, T. Velusamy, G. Jain, et al., Synthesis of copper-based nanostructures in liquid environments by means of a non-equilibrium atmospheric pressure nanopulsed plasma jet, Plasma Chem. Plasma Process. 38 (6) (2018) 1209–1222.
[51] C. Ni, D. Carolan, C. Rocks, J. Hui, Z. Fang, D.B. Padmanaban, et al., Microplasma-assisted electrochemical synthesis of Co 3 O 4 nanoparticles in absolute ethanol for energy applications, Green. Chem. 20 (9) (2018) 2101–2109.
[52] R. McGlynn, S. Chakrabarti, B. Alessi, H.S. Moghaieb, P. Maguire, H. Singh, et al., Plasma-induced non-equilibrium electrochemistry synthesis of nanoparticles for solar thermal energy harvesting, Sol. Energy [Internet] 203 (2020) 37–45, https://doi.org/10.1016/j.solener.2020.04.004 (Available from), ⟨http://www.sciencedirect.com/science/article/pii/S0038092×20303790⟩.
[53] C. Ni, D. Carolan, J. Hui, C. Rocks, D. Padmanaban, J. Ni, et al., Evolution of anodic product from molybdenum metal in absolute ethanol and humidity sensing under ambient conditions, Cryst. Growth Des. 19 (9) (2019) 5249–5257.
[54] S. Chakrabarti, D. Carolan, B. Alessi, P. Maguire, V. Svrcek, D. Mariotti, Microplasma-synthesized ultra-small NiO nanocrystals, a ubiquitous hole transport material, Nanoscale Adv. 1 (12) (2019) 4915–4925.

[55] D.B. Padmanaban, R. McGlynn, E. Byrne, T. Velusamy, M. Swadźba-Kwaśny, P. Maguire, et al., Understanding plasma–ethanol non-equilibrium electrochemistry during the synthesis of metal oxide quantum dots, Green. Chem. 23 (11) (2021) 3983–3995.

[56] R.V. Siriwardane, J.A. Poston, Characterization of copper oxides, iron oxides, and zinc copper ferrite desulfurization sorbents by X-ray photoelectron spectroscopy and scanning electron microscopy, Appl. Surf. Sci. 68 (1) (1993) 65–80.

[57] W. Wang, Z. Liu, Y. Liu, C. Xu, C. Zheng, G. Wang, A simple wet-chemical synthesis and characterization of CuO nanorods, Appl. Phys. A. 76 (3) (2003) 417–420.

[58] J.F. Xu, W. Ji, Z.X. Shen, W.S. Li, S.H. Tang, X.R. Ye, et al., Raman spectra of CuO nanocrystals, J. Raman Spectrosc. 30 (5) (1999) 413–415.

[59] M.C. Biesinger, L.W.M. Lau, A.R. Gerson, R.S.C. Smart, Resolving surface chemical states in XPS analysis of first row transition metals, oxides and hydroxides: Sc, Ti, V, Cu and Zn, Appl. Surf. Sci. 257 (3) (2010) 887–898.

[60] M.C. Biesinger, Advanced analysis of copper X-ray photoelectron spectra, Surf. Interface Anal. 49 (13) (2017) 1325–1334.

[61] Y. Cudennec, A. Lecerf, The transformation of Cu (OH) 2 into CuO, revisited, Solid State Sci. 5 (11–12) (2003) 1471–1474.

[62] I.V. Morozov, K.O. Znamenkov, Y.M. Korenev, O.A. Shlyakhtin, Thermal decomposition of Cu (NO3) 2·3H2O at reduced pressures, Thermochim. Acta 403 (2) (2003) 173–179.

[63] A. Standard, G173-03-standard tables for reference solar spectral irradiances: direct normal and hemispherical on 37 tilted surface, Ann. Book ASTM Stand. 2003 14 (2012).

[64] M.A. Rafea, N. Roushdy, Determination of the optical band gap for amorphous and nanocrystalline copper oxide thin films prepared by SILAR technique, J. Phys. D: Appl. Phys. 42 (1) (2008) 15413.

[65] T. Zhang, Q. Zou, Z. Cheng, Z. Chen, Y. Liu, Z. Jiang, Effect of particle concentration on the stability of water-based SiO2 nanofluid, Powder Technol. 379 (2021) 457–465.

[66] M. Ma, Y. Zhai, P. Yao, Y. Li, H. Wang, Effect of surfactant on the rheological behavior and thermophysical properties of hybrid nanofluids, Powder Technol. 379 (2021) 373–383.

[67] V.A. Martínez, F. Lozano-Steinmetz, D.A. Vasco, P.A. Zapata, I. Chi-Durán, D. P. Singh, Thermal characterization and stability analysis of aqueous ZnO-based nanofluids numerically implemented in microchannel heat sinks, Therm. Sci. Eng. Prog. 22 (2021), 100792.

[68] X. Chen, Z. Xiong, M. Chen, P. Zhou, Ultra-stable carbon quantum dot nanofluids for direct absorption solar collectors, Sol. Energy Mater. Sol. Cells [Internet] (240) (2022), 111720, https://doi.org/10.1016/j.solmat.2022.111720 (Available from), ⟨https://www.sciencedirect.com/science/article/pii/S0927024822001416⟩.

[69] D. Qu, L. Cheng, Y. Bao, Y. Gao, X. Zheng, G. Qin, Enhanced optical absorption and solar steam generation of CB-ATO hybrid nanofluids, Renew. Energy 199 (2022) 509–516.

[70] O.Z. Sharaf, N. Rizk, C.P. Joshi, M. Abi Jaoudé, A.N. Al-Khateeb, D.C. Kyritsis, et al., Ultrastable plasmonic nanofluids in optimized direct absorption solar collectors, Energy Convers. Manag. 199 (2019), 112010.

[71] O.Z. Sharaf, N. Rizk, C.J. Munro, C.P. Joshi, D.H. Anjum, E. Abu-Nada, et al., Radiation stability and photothermal performance of surface-functionalized plasmonic nanofluids for direct-absorption solar applications, Sol. Energy Mater. Sol. Cells 227 (2021), 111115.

[72] T.J. Choi, S.P. Jang, M.A. Kedzierski, Effect of surfactants on the stability and solar thermal absorption characteristics of water-based nanofluids with multi-walled carbon nanotubes, Int. J. Heat. Mass Transf. 122 (2018) 483–490.